

## BIOMIMETICS

# Bird-inspired reflexive morphing enables rudderless flight

Eric Chang<sup>1</sup>, Diana D. Chin<sup>1</sup>, David Lentink<sup>2\*</sup>

Gliding birds lack a vertical tail, yet they fly stably rudderless in turbulence without needing discrete flaps to steer. In contrast, nearly all airplanes need vertical tails to damp Dutch roll oscillations and to control yaw. The few exceptions that lack a vertical tail either leverage differential drag-based yaw actuators or their fixed planforms are carefully tuned for passively stable Dutch roll and proverse yaw. Biologists hypothesize that birds stabilize and control gliding flight without rudders by using their wing and tail reflexes, but no rudderless airplane has a morphing wing or tail that can change shape like a bird. Our rudderless biohybrid robot, PigeonBot II, can damp its Dutch roll instability (caused by lacking a vertical tail) and control flight by morphing its biomimetic wing and tail reflexively like a bird. The bird-inspired adaptive reflexive controller was tuned in a wind tunnel to mitigate turbulent perturbations, which enabled PigeonBot II to fly autonomously in the atmosphere with pigeon-like poses. This work is a mechanistic confirmation of how birds accomplish rudderless flight via reflex functions, and it can inspire rudderless aircraft with reduced radar signature and increased efficacy.

## INTRODUCTION

Unlike airplanes, birds can glide rudderless (1) by morphing the shapes of their wings and tails continuously (2, 3). In contrast, airplanes generally achieve longitudinal (pitch) stability with a horizontal tail and lateral-directional (roll and yaw) stability with wing dihedral and a vertical [or V-shaped (4)] tail that works like a weathercock (5) (pitch, roll, yaw: Fig. 1A). Similar to the early flight pioneers (6), today's pilots use horizontal tail elevators to pitch, wing ailerons to roll, and vertical [or V (4)] tail rudders to yaw (5). Because pitch can also be stabilized using wing sweep or reflexed camber airfoils, horizontal tails are not essential and can be removed (7). However, eliminating vertical tails poses several challenges. Although aircraft wings with carefully tuned sweep can achieve weathercock stability without a vertical tail, birds can achieve this for any wing sweep including nonswept wings, which suggests that they harness a more versatile solution that is applicable to an exceptionally wide range of (morphing) wing planforms. Further, airplanes need to generate yaw moments to coordinate turns and reject yaw disturbances. A vertical tail rudder is the conventional solution, given that it generates the required yaw moments with lift pointing sideways, which is aerodynamically more efficient than using differential drag. Notably, when a vertical tail is incorrectly sized on or removed from an otherwise stable configuration, airplanes experience Dutch roll instability, rolling and yawing approximately 90° out of phase, which demands active yaw rate damping with a yaw actuator (5, 8). Consequently, the rare airplanes that lack a vertical tail either use differential drag-based actuators (split flaps or differential spoilers) to control yaw [like Horten (9) and the B2 (7)] or have specially tuned wing geometries for passive static and dynamic lateral stability and proverse yaw [like NASA's Prandtl wing (10)]. In contrast, birds appear to achieve rudderless flight more efficiently and flexibly without reliance on drag-based actuators and with a large diversity of wing planforms and dihedral. Despite substantial advances made with numerous designs, avian-inspired morphing wing and tail robots have

struggled to demonstrate sustained autonomous flight without a vertical tail (table S1). Unraveling how birds achieve this feat could inspire uncrewed autonomous vehicles and aircraft with increased efficacy and reduced radar signature.

Gliding birds are thought to achieve stability and control by combining wing and tail neuromuscular reflexes that mitigate disturbances with intentional muscle-driven motions that control flight (11). However, these reflexes have been studied in nonflying birds (11–15), and reflexive and intentional control remains indistinguishable in vivo (11). Pigeons display remarkably consistent reflexes when their trunk is rolled (longitudinal axis), pitched (transversal), or yawed (dorsoventral) manually or with an apparatus (11, 16, 17). Notably, the reflexes are stronger when air is blown on their breast's mechanosensory filoplumes to simulate flight (17). In 1929, Groebbs postulated that these reflexes enable birds “to function as automatically controlled airplanes” (11, 18). Since then, wing and tail reflexes have been aerodynamically interpreted to stabilize flight (11–15, 17). Our aerodynamic simulation of pigeon morphed wing (19) and tail (figs. S4 and S5) configurations and other analyses (20, 21) support this. However, demonstrating a reflex-based control scheme that can stabilize bird-inspired morphing wing and tail configurations during sustained autonomous flight without a vertical tail is an open challenge (table S1). The reflexive control hypothesis is contrasted by findings with fixed-wing radio-controlled (RC) models that show that biomimetic wing dihedral combined with prominent wingtip slots offer sufficient passive stability to damp Dutch roll in soaring birds (22, 23). However, in nature, soaring birds continuously morph their tail (24), and pigeons glide with a wide range of wing sweeps without prominent wingtip slots (25), which suggests reflexive control for stabilizing flight instabilities including Dutch roll.

In this article, we developed a biomimetic morphing wing and tail robot model (PigeonBot II) to test the biological hypothesis that birds can automatically control and stabilize their flight with morphing wing and tail reflexes and to create a flight-demonstrated engineering model that shows how robots can accomplish rudderless flight by harnessing autonomous reflexive morphing. We first established that pigeon-like rudderless planforms are Dutch roll unstable (Fig. 2 and movie S2). By tuning our bird-inspired reflexive

<sup>1</sup>Department of Mechanical Engineering, Stanford University, Stanford, CA, USA. <sup>2</sup>Faculty of Science and Engineering, University of Groningen, Groningen, Netherlands.

\*Corresponding author. Email: d.lentink@rug.nl

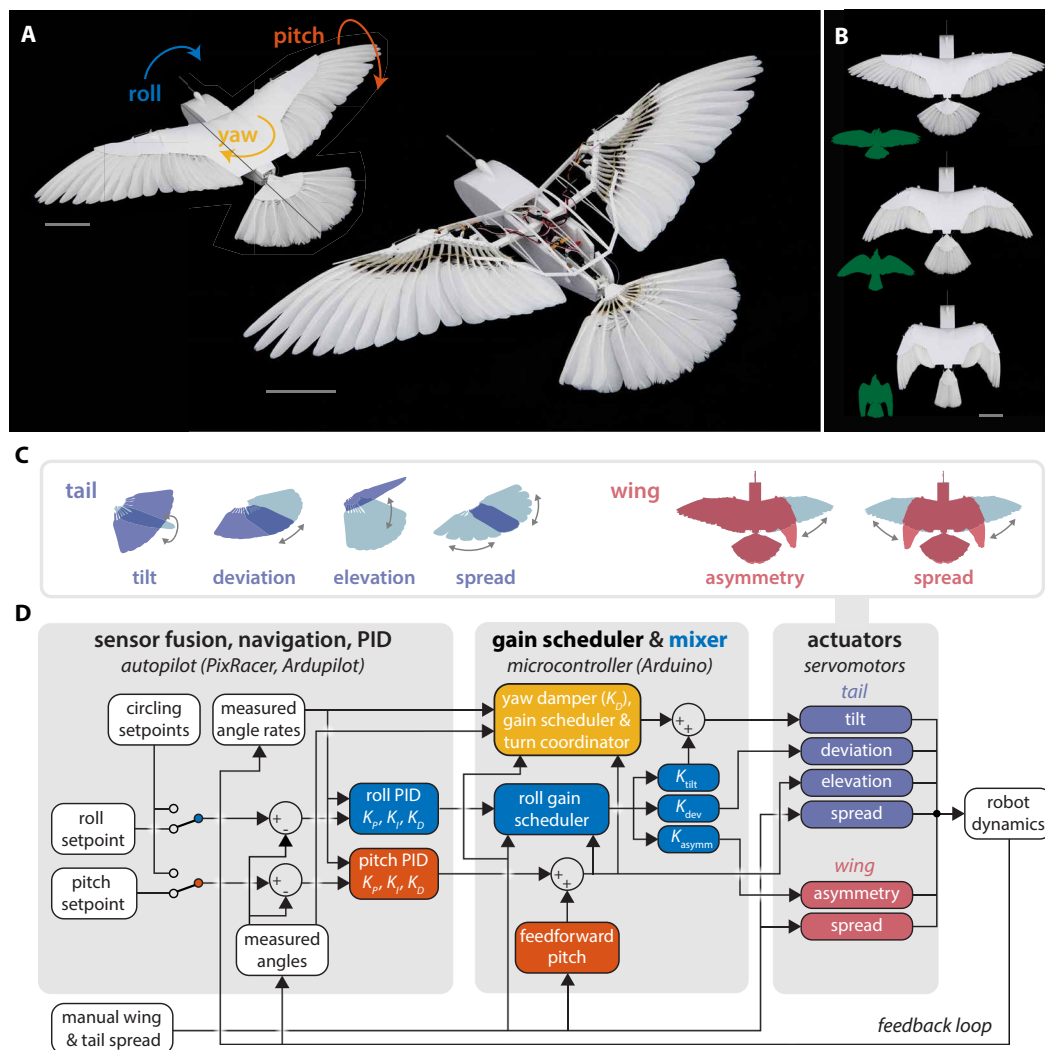


**Fig. 1. PigeonBot II morphs its wing and tail reflexively to fly rudderless autonomously.** (A) Biomimetic skeleton and connective elastic ligaments underactuate the wing's 40 remiges with four servomotors (two wrists and two second digits) and the tail's 12 feathers with five servomotors (movie S3). Scale bars, 100 mm. (B) Wing and tail can be arbitrarily morphed; shown here are three typical pigeon postures during gliding (green) with the wing and tail approximately proportionally morphed from spread to middle to tucked (25). Scale bar, 100 mm for PigeonBot II photos. (C) Avatars illustrate the six controlled tail and wing morphing DOFs used in this study. (D) Reflexive control loop for autonomous controlled flight in the atmosphere based on sensor fusion-based body angle and angular rate feedback: Pitch is controlled with tail elevation; roll is controlled with wing asymmetry, tail tilt, and lateral deviation; and the yaw rate is damped with tail tilt (movie S4). To navigate the robot, the teleoperator inputs an airspeed setpoint and either high-level roll and pitch setpoints via radio or switches to autonomous circling setpoints. The autopilot then computes conventional roll, pitch, and yaw commands with PID control. Next, a microcontroller adapts the output with fitted gains tuned for all morphing wing and tail permutations (spread, middle, and tucked). Last, the roll command is mixed  $[K_{\text{asymm}}, K_{\text{dev}}, K_{\text{tilt}}] = [1, 2, 1/4]$  and mapped to the servomotors to reflexively morph the wing and tail.

controller (Fig. 1D) in a virtual flight-testing setup in a wind tunnel, we found that appropriate mixing of wing asymmetry, tail tilt, and tail lateral deviation in response to roll perturbations maximizes roll tracking (Figs. 2 and 3) and stability in turbulence (Fig. 4) across wing and tail spread permutations. Using the reflexive controller tuned in the wind tunnel, we tested PigeonBot II during autonomous atmospheric flights to demonstrate robust flight stabilization and navigation at near-proportional wing and tail spread morphing combinations (Fig. 5 and movie S7). This work confirms how birds can accomplish rudderless flight via reflex functions, and it can inspire rudderless aircraft with reduced radar signature and increased efficacy.

## RESULTS

### Bird-inspired reflexive tail morphing alone is insufficient

To dynamically test whether reflexive tail morphing alone could suppress Dutch roll in flight, we first developed a biohybrid “TailBot.” TailBot features an intermediately spread pigeon wing planform made from foamboard with dihedral, combined with a tail with 12 elastically connected pigeon feathers that can be actively furled and unfurled symmetrically (and optionally asymmetrically), elevated and depressed, tilted to either side, and moved laterally left or right (movie S1 and figs. S1 and S2). Among these five degrees of freedom (DOFs), tail tilt stands out because it generates yaw torque [figs. S4 and S5 (20, 21)], which we confirmed with measurements

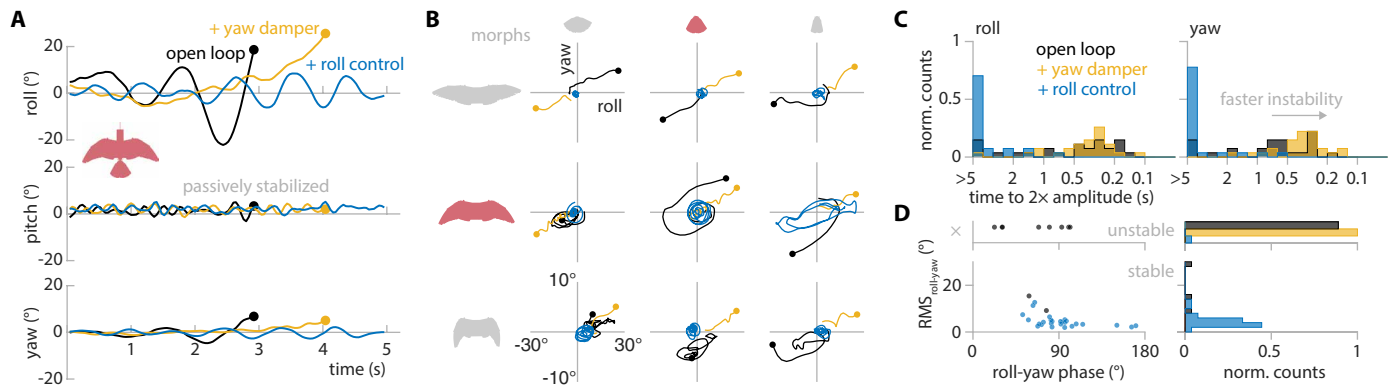


**Fig. 2. Reflexive wing and tail morphing damps Dutch roll sufficiently.** (A and B) We mounted PigeonBot II on a ball bearing to roll, pitch, and yaw freely in the wind tunnel with tail elevation set to passively stabilize pitch at the cruise AoA. Shown are the angular dynamics after release from its symmetric cruise position using the final autonomous flight mixer values  $[K_{\text{asymm}}, K_{\text{dev}}, K_{\text{tilt}}] = [1, 2, \frac{1}{4}]$ . The open-loop (black) case shows that the biomimetic wing dihedral and biohybrid tip slots damp Dutch roll insufficiently, which a vertical tail can resolve (movie S2). Adding aircraft-inspired yaw damping (yellow) reduces oscillation but still diverges like spiral divergence in airplanes (5, 8). Adding full (yaw damper + roll control) reflexive control (blue) damps Dutch roll instability sufficiently. The yaw-roll phase space plots (B) show that reflexive yaw and roll control (blue) suffice for all but the middle-wing tucked-tail morph case. The full control residual is mostly roll (yaw axis stretched three times). (C) Time to double amplitude is mitigated with full (blue) control. (D) Phase differences between roll and yaw center around 90° and correspond to the Dutch roll residual. [(C) and (D)] Distributions pooled across all nine morphs and three AoAs; incomputable phase differences not shown.

from TailBot's inertial measurement unit (IMU). We chose to use real pigeon feathers for TailBot, similar to our previous biohybrid morphing wing work, because of flight feathers' abilities to directionally fasten even when perturbed with turbulence (3). In addition, feathers provide favorable elastic stiffness-dominated dynamics, soft edges that continuously slide and aerodynamically close the morphing surface, and the ability to be easily repaired by preening them by hand (19). We considered artificial feathers made from fiber-reinforced composites (26, 27) and three-dimensional (3D) printing, but none of these exhibited the favorable characteristics [such as probabilistic fastening (28) and the unusual softness and lightness] offered by real feathers. Airplane theory shows that Dutch roll can be controlled by the damping yaw rate (5, 8), so we programmed TailBot to damp changes in its body yaw rate by adjusting its tail tilt reflexively (figs. S4 and S5). Virtual flight experiments with TailBot mounted on a three-DOF ball bearing (free roll, pitch, and yaw; translations locked, see the Supplementary Methods) in our wind tunnel (29) confirmed Dutch roll instability as soon as its backup vertical tail was retracted (movie S2). Reflexive tail tilt effectively damped Dutch roll. Maintaining symmetric flight conditions required combining it with proportional, integral, and derivative (PID) roll error control mapped to tail tilt and tail deviation and pitch PID control mapped to tail elevation. Combined, they mitigated aileron-induced roll perturbations during virtual flight using only tail tilt, deviation, and elevation. However, TailBot's atmospheric flights included large roll oscillations (movie S2) and crashes due to limited tail roll control authority.

### PigeonBot II: Biohybrid wing and tail morphing robot with reflexive control

To mitigate TailBot's large roll oscillations during atmospheric flight, we incorporated our articulated PigeonBot morphing wing design. It includes pigeon wingtip slots and a wing dihedral (19) that should aid in damping Dutch roll (22, 23). Our previous PigeonBot demonstrated asymmetric wing morphing to control roll but still used a

conventional horizontal and vertical tail to control pitch and yaw (19). PigeonBot II (Fig. 1, A and B) combines wing and tail morphing (Fig. 1C) to fully replace conventional airplane control (movie S3; for design, see Materials and Methods). Its 52 pigeon flight feathers rotate to morph continuously when underactuated by nine servomotors. The total in-flight mass of PigeonBot II is ~300 g, on par with pigeons. Its nonbiomimetic propulsion, two small propellers mounted on each wrist, enables it to ascend, cruise, circle, and descend teleoperated in different pigeon gliding poses (motors removed during wind tunnel experiments; fig. S3). We selected a PID control scheme for our reflexive control loop (Fig. 1D) to have a well-substantiated minimal model that mimics pigeon reflexes that are observed to respond proportionally to angular perturbations in accordance with the putative PID-like sensorimotor attitude control loop developed for bird flight by Bilo (11). To do so, we incorporated combined roll-induced wing asymmetry (11) and tail deviation (17) (including tail tilt for robustness), as well as pitch-induced tail elevation (11, 17) [excluding wing (11) and tail (16) spread for simplicity]. Pigeon reflex recordings show a near-zero tail tilt response to yaw angle (17), so we set the yaw angle proportional control gain  $K_P$  and integral control gain  $K_I$  to zero. We implemented only yaw angle derivative control ( $K_D$ ) so that PigeonBot II's (and TailBot's) tail tilt reflex responded directly to the yaw rate, enabling it to damp Dutch roll (movies S2 and S5). Although an experiment demonstrating a yaw rate damping reflex in vivo has yet to be performed, observations of tail tilt in maneuvering birds (24) and TailBot and PigeonBot II wind tunnel experiments suggest that tail tilt functions as a yaw rate-induced reflex in birds. To implement our pigeon-inspired autonomous reflexive control (movie S4) in atmospheric flights, we augmented a conventional autopilot by first multiplying the pitch, roll, and yaw outputs with our adaptive gain scheduler. It fits gains tuned in the wind tunnel as second-order polynomial models (Materials and Methods) across all three-by-three wing and tail morphing posture (spread, middle, tucked) and three angle-of-attack (AoA; cruise, cruise +3°, cruise -3°) combinations. Next, the control

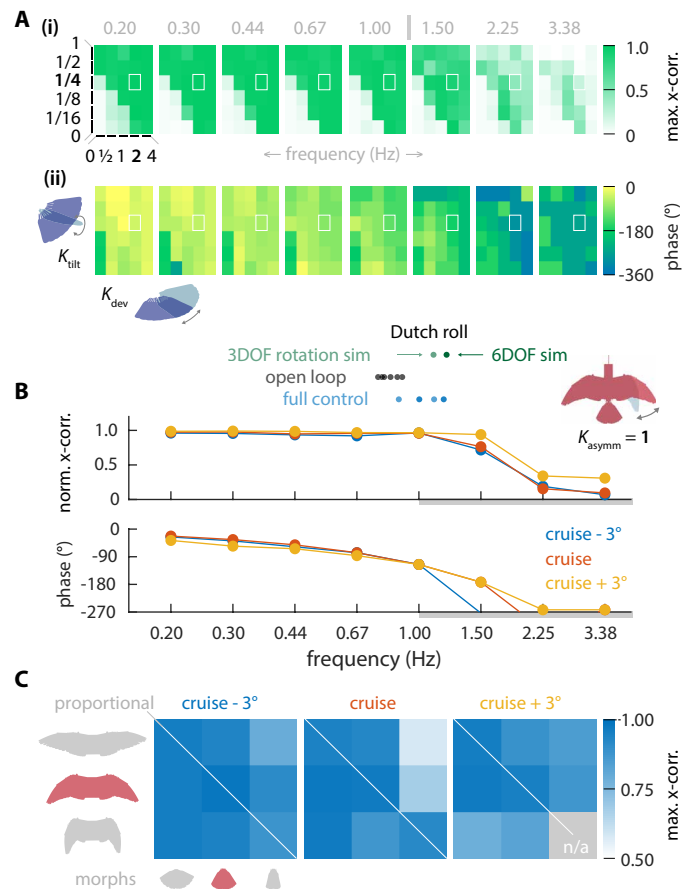


**Fig. 3. Coordinated roll requires mixing wing asymmetry with substantial tail tilt and deviation.** (A) During tracking of a sinusoidal roll command in the middle-middle morph cruise case, maximal cross (x) correlation (i) and minimal phase lag (ii) are accomplished by mixing wing asymmetry ( $K_{\text{asym}} = 1$ ) with high tail tilt ( $K_{\text{tilt}}$ ) and/or deviation ( $K_{\text{dev}}$ ). Tracking deteriorates beyond 1 Hz. For all subsequent tests, we mixed wing asymmetry,  $K_{\text{asym}} = 1$ , with tail tilt,  $K_{\text{tilt}} = 0.25$ , and deviation,  $K_{\text{dev}} = 2$  (denoted by the white box), which tracks the roll angle most robustly. (B) Bode plots show that PigeonBot II's servo-actuated control roll-off occurs beyond 1 Hz ( $-180^\circ$  phase error), which enables the effective bandwidth of the controller to overlap with most of the measured (residual) Dutch roll frequencies (circles; cruise, cruise +  $3^\circ$ , and cruise -  $3^\circ$  data pooled) and simulated three-DOF rotational (as in virtual flight testing) and six-DOF rotational and translational (as in free flight) Dutch roll frequencies. (C) Near-proportional wing-tail morphing combinations (diagonal) track sinusoidal roll well (averaged across frequencies of  $\leq 1$  Hz) around ( $\pm 3^\circ$ ) trimmed cruise AoAs (n/a: not tested, tail volume too small to trim cruise +  $3^\circ$ ).

commands are mixed to embody coupled pigeon reflexes: Roll is mixed to actuate wing asymmetry ( $K_{\text{asym}}$ ), tail lateral deviation ( $K_{\text{dev}}$ ), and tail tilt ( $K_{\text{tilt}}$ ); the pitch command only actuates tail elevation; and the yaw command only actuates tail tilt. Last, the commands are mapped to change the angle of the nine servomotors that morph PigeonBot II.

### Reflexive wing asymmetry mixed with tail tilt and deviation damps Dutch roll

Virtual flight tests with PigeonBot II in the wind tunnel (movie S5 and fig. S6) show unstable dynamics when operated open loop (without active control) and when using airplane-inspired yaw

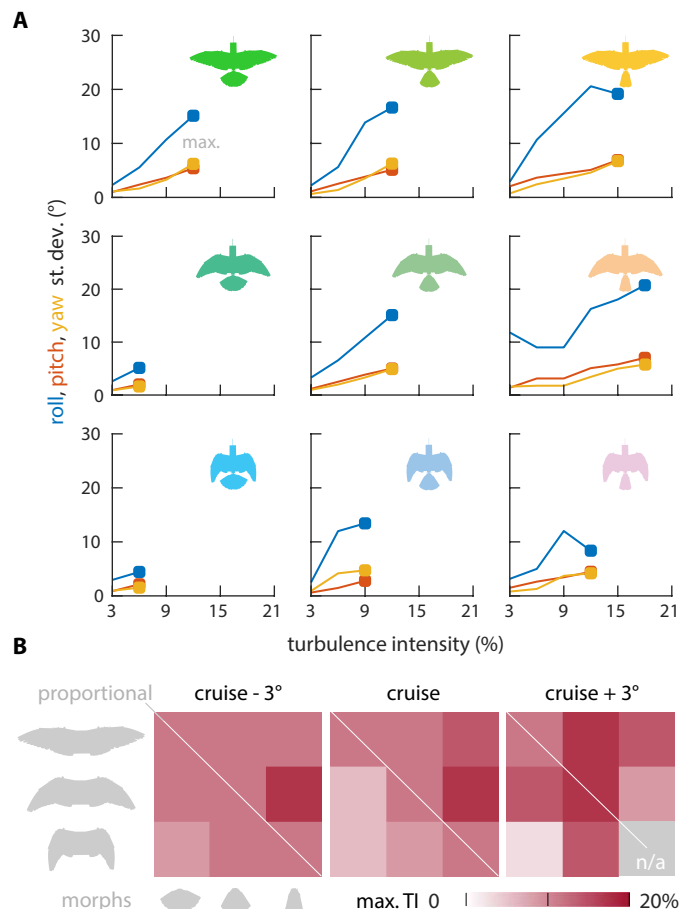


**Fig. 4. Turbulence intensity bounds closed-loop rudderless flight control.** Turbulence intensity was controlled by our turbulence generation system (29, 47) and ranged from 3 to 21%. (A) Wind tunnel turbulence intensity boundaries at which PigeonBot II (with pitch passively stabilized) can no longer mitigate roll and yaw divergence with closed-loop reflexive control (movie S6). All experiments started at symmetric cruise conditions with steady-level cruise setpoints perturbed by turbulence. See the “Statistical analysis” section in Materials and Methods for details on calculating the SD. (B) Near-proportional wing-tail morphing combinations (diagonal) mitigate turbulence well (n/a: not tested, tail volume too small to trim cruise +  $3^\circ$ ).

damping, which results in spiral-like divergence (Fig. 2, A and B) (5, 8). To evaluate whether our three-DOF wind tunnel setup could reasonably capture the same stability dynamics expected during outdoor six-DOF flight, we compared simulated six-DOF versus three-DOF dynamics for each of PigeonBot II's three-by-three wing and tail morph configurations (see Supplementary Methods). Our simulations show that the three-DOF virtual flight test setup in the wind tunnel (free pitch, roll, and yaw with locked translational motion) reasonably approximates Dutch roll dynamics during full six-DOF free flight (fig. S7). The linearized Dutch roll equations show an average difference (six DOFs versus three DOFs) in Dutch roll frequency of 13% and a time-to-double amplitude of 11% (fig. S8). Therefore, the recorded dynamics of PigeonBot II during three-DOF virtual flight testing sufficiently represent the same Dutch roll characteristics as in six-DOF free flight for tuning the autonomous reflexive control loop without crashing the robot. This approach



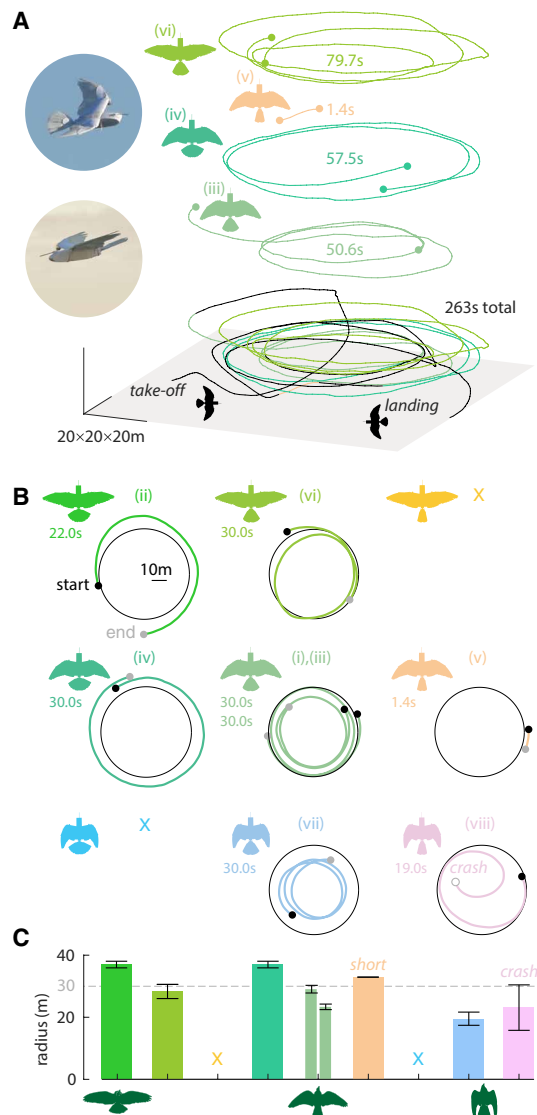


**Fig. 5. PigeonBot II flies autonomously with reflexive wing and tail morphing.**

PigeonBot II reflexively morphs autonomously to attain high-level navigation roll and pitch setpoints received by radio (teleoperated) or from its fixed-radius circling setpoints (movie S7). The teleoperator manually sets the wing and tail morph configurations. (A) Autonomous reflexive flight control commences with take-off teleoperated in middle-middle morph. When cruise conditions are reached, its autonomous circling performance is assessed for the different morph permutations (spread, middle, and tucked). It lands again teleoperated in middle-middle morph. Shown is the autonomous flight sequence from take-off to landing (black) including circle tests (iii) to (vi) (colored tracks; copies are projected above the flight track for perusal) with autonomous segments before and after circling. (B) Autonomous circling segments, tests commenced as numbered (i) to (viii). The middle-tucked morph case (v) was aborted early because of insufficient pitch authority causing PigeonBot II to descend rapidly and gain speed beyond its tuned airspeed range. The tucked-tucked morph case (viii), which could not be trimmed at a cruise angle  $+3^\circ$  in the wind tunnel, spiraled into a nosedive crash that concluded flight testing. The tucked-middle morph test case (vii) shows that a larger tail volume is sufficient for stabilizing PigeonBot II with tucked wings during circling. (C) Commanded circling radius tracking performance is reasonable across all tested morph combinations (bars show the mean circle radius, and error bars show the SD of the circle radius for each flight segment as defined in Materials and Methods). Avatars indicate the wing/tail area ratios that pigeons approximately adopt during gliding (25).

resolved unstable open-loop Dutch roll in the wind tunnel by implementing closed-loop reflexive morphing control with appropriate mixing gains tuned for each individual morph case (fig. S9), which reduces the time-to-double roll/yaw amplitude by more than an order of magnitude (Fig. 2C). It also reduces the Dutch roll root mean square (RMS) amplitude (with roll-yaw phase differences centered around  $90^\circ$ ) to a manageable residual (Fig. 2D), as in airplanes (8). To determine these wing and tail morphing mixing gains, we assessed the roll tracking performance for a  $15^\circ$  sinusoidal (left-right) roll command across a 10-fold frequency range (Fig. 3A and fig. S10). We found that commanding only wing asymmetry [ $K_{\text{dev}}$ ,  $K_{\text{tilt}}$ ] = [0, 0] fails tracking at all frequencies (Fig. 3A). Mixing only tail tilt ( $K_{\text{dev}} = 0$ ) or lateral deviation ( $K_{\text{tilt}} = 0$ ) with wing asymmetry ( $K_{\text{asymm}} = 1$ ) fails up to intermediate gains and, thus, requires either high  $K_{\text{tilt}}$  or  $K_{\text{dev}}$  gains. Mixing tail tilt and deviation combined with wing asymmetry tracks roll more robustly. We thus selected gains that leverage all three DOFs in our reflex mixer (Fig. 1D): [ $K_{\text{asymm}}$ ,  $K_{\text{dev}}$ ,  $K_{\text{tilt}}$ ] = [1, 2,  $\frac{1}{4}$ ] (white box, Fig. 3A). The reflexive roll tracking performance is robust at or below 1 Hz (Fig. 3, A and B), which enables the bandwidth of the controller to overlap with the measured Dutch roll frequencies (Fig. 3B). Previous tests with this wing show that the controller bandwidth is limited by microservomotor saturation (19); roll control is thus marginal and wing actuator limited. Regardless, PigeonBot II sufficiently tracks sinusoidal roll across wing and tail morph combinations for all three AoAs (cruise, cruise  $+3^\circ$ , cruise  $-3^\circ$ ; Fig. 3C).

### Mixed wing and tail reflexes are robust to moderate turbulence intensity

PigeonBot II's reflexive controller gains are robust to moderate turbulence intensities across morph configurations (Fig. 4A). Notably, pigeon-like proportional morphed wing and tail configurations (Fig. 1B) performed consistently up to  $\sim 12\%$  turbulence intensity (movie S6 and fig. S12). Across all experiments, the roll standard deviation (SD) reached the highest values when perturbed by turbulence, consistent with wing servomotor saturation (19). Comparing turbulence robustness across all three-by-three wing and tail morph combinations for three trimmed AoAs (cruise, cruise  $+3^\circ$ , cruise  $-3^\circ$ ; Fig. 4B), we found that proportional wing and tail configurations are robust. As in the roll tracking test (Fig. 3C), the proportional tucked-tucked configuration could not be trimmed at the cruise  $+3^\circ$  AoA. In contrast, the middle-tucked and tucked-middle configurations were trimmable at  $+3^\circ$ , suggesting that these configurations should be more robust. However, the wind tunnel tests of TailBot (movie S2) did not fully predict atmospheric flight performance.

### Reflexive morphing enables autonomous rudderless flight

PigeonBot II's atmospheric flight tests show that its autonomous reflexive controller enables a teleoperator to take off, cruise, and land in proportional (diagonal) and approximately proportional (near-diagonal) wing and tail morph configurations on the basis of high-level roll and pitch setpoints (Fig. 5A, fig. S17, and movie S7). All flight phases required and demonstrated fully autonomous reflexive control. Autonomous circling was satisfactory in all cases except middle-wing tucked-tail, which descends too fast, and tucked-wing tucked-tail, which spirals down after initiating autonomous circling, due to insufficient pitch authority (Figs. 3C and 4B and figs. S13 and S14). Successful autonomous circling of the tucked wing combined

with the middle tail morph confirms that a larger tail volume resolves the instability (Fig. 5B and fig. S15). Compared with a pigeon, the tucked-tail area of PigeonBot II is proportionally too small compared with its tucked wing because its wing lacks the biomimetic humerus and patagium needed to tuck further (19), whereas its tail is tucked more than a pigeon tail (fig. S16A). Given that pigeons adopt approximately proportional wing and tail morph combinations during gliding (Fig. 1B (25)), we did not further test the extremely disproportional morphed configurations (spread-tucked, tucked-spread). By comparing the target and achieved autonomous circling radii (Fig. 5B) and roll angles (figs. S13 to S15 and S17), we concluded that servomotor roll-off (Fig. 3, A and B) limits both the controllability and accuracy of reflexive morphing flight control. Nevertheless, the rudderless flights of PigeonBot II show that its autonomous reflexive morphing control loop is effective despite its near-saturated wing actuators. Future robots could probably automatically recover from the control authority loss observed in the tucked-tucked circling experiment by reflexively returning to the robust middle-middle morph (Fig. 5, A and B), just as pigeons respond to pitching down motions with forward wing-sweep (11) and tail spread reflexes (16). This is supported by our successful teleoperated recovery of the diving middle-wing tucked-tail morph (Fig. 5, A and B) by switching it back to the middle-tail morph. Birds thus not only sweep their wings to improve glide performance (30), but also maintain flight control by covarying tail spread [(25), fig. S16].

## DISCUSSION

Inspired by how birds glide stably in turbulence without a vertical tail, we developed PigeonBot II with 52 underactuated wing and tail feathers to find and validate a minimal mechanistic model for rudderless flight on the basis of reflexive morphing control. We established that pigeon-like planforms are Dutch roll unstable when they do not have a vertical tail (movie S2 and fig. S7). Applying reflexive tail tilt resolved Dutch roll in virtual flight testing on a ball bearing in the wind tunnel but was insufficient for stable flights in the atmosphere. We therefore added reflexive wing morphing and found that appropriate mixing of wing asymmetry, tail tilt, and tail lateral deviation maximizes roll tracking performance across wing and tail spread permutations (Figs. 2 and 3). By adding turbulence in the wind tunnel, this control scheme enabled stable flight up to 12% turbulence intensity at near-proportional wing and tail spread morphing combinations (Fig. 4). Last, we conducted untethered atmospheric flights to demonstrate that this autonomous reflexive control scheme achieves flight attitude stabilization and enables fully autonomous circling flight navigation for a variety of wing and tail poses (Fig. 5). Our roll tracking, turbulence, and atmospheric flight tests demonstrated that our reflexive control strategy was most robust at near-proportional wing and tail spread morphing combinations. This helps explain the observed behavioral envelope of pigeons preferring to glide with approximately proportionally morphed wings and tails (avoiding disproportional morphing like spread wings with tucked tails and vice versa; fig. S16) (25).

Our wind tunnel and atmospheric flight experiments with PigeonBot II corroborate the functional interpretation of reflexes studied in nonflying birds (11, 13–15, 17, 31) and support Groebbel's hypothesis that reflexes enable automatically controlled flight in birds (18). The bird-inspired reflexive control loop also suggests a key role for bird tail tilt in damping yaw rate. Whereas previous tail

tilt reflex experiments in pigeons only tested yaw angle and found no reflex gain (17), we hypothesized that the yaw rate will show reflex gain. In addition, our test outcomes challenged the idea that soaring birds damp Dutch roll solely passively by combining wing dihedral with wingtip slots (22, 23). New biohybrid robots embodying the diversity in bird aeromechanic parameters (32) could unravel this. Further, integrating a central pattern generator to model intentional control (11) can enable distinguishing reflex and intentional flight control performance (33).

The bird-inspired control principles can also inform the design of rudderless airplanes with minimal radar signature and elevated maneuverability and efficiency (20, 34); they should mix tail tilt with aileron actuation and, when structurally feasible, tail deviation. Previous examples of rudderless airplanes required drag-based active directional control systems and/or carefully designed planforms with wing sweep, twist, and a dihedral tuned to favorable lateral stability characteristics and proverse yaw (10, 35, 36). In contrast, our bird-inspired reflexive control method can be applied to a much broader range of morphing wing and tail planforms, which opens the potential to improve efficiency and maneuverability while simultaneously decreasing the radar cross section. For instance, wing sweep and twist required for passive stability can be reduced with a larger tail control surface for equivalent drag, and vertical tail drag [as in conventional aircraft (5, 7, 8)] and drag-based yaw control such as split flaps [as in flying wings (7)] can be eliminated entirely. More involved rudderless flight stabilization methods such as active wing flapping (37) or variable wing dihedral (38) are less practical at the scale of airplanes.

In this work, we designed our reflexive feedback loops as basic PID control loops with gain scheduling and mixed wing and tail morphing in response to IMU feedback (Fig. 1D), which enabled fast tuning, a rich variety of experimental variations, and a tractable path to atmospheric flights while still being representative of neuroscience observations of proportional pigeon reflexes (11, 16, 17). More advanced control techniques, such as nonlinear model-based and optimal control (39) could unleash further maneuverability and disturbance rejection performance gains for future rudderless flight vehicles. Modern control techniques such as artificial, or even spiking, neural networks could enable model-free control approaches that more closely mimic biological processing (40) and augment our reflexive control approach with a greater diversity of sensing. These controllers may be well positioned for integrating other sensing modalities, such as bird-inspired distributed air flow sensors mimicking filoplumes (17) to actively avoid stall. Last, innovation is needed to develop new micro actuators on par with bird muscles (41, 42) that control morphing at 10-fold higher frequencies than Dutch roll for exceptional rudderless morphing flight control.

## MATERIALS AND METHODS

### TailBot design and fabrication

TailBot's tail morphing mechanism used five Dymond D47 servomotors to actuate 12 pigeon (*Columba livia*) tail feathers. Pigeon tail feathers (left and right R1–R6) were used in their corresponding locations in the robot mechanisms. We used a combination of push-rods (for elevation, 0.9-mm music wire), a push-pull Bowden cable (for spread and lateral deviation, 0.30-mm music wire) in polytetrafluoroethylene tubing (0.31-mm internal diameter), and a torque tube (for tail tilt, 4-mm carbon fiber tube) to actuate the feathers

while keeping the mass close to the center of gravity (CG). One servo actuated each outermost feather to accomplish spread (two total), so although asymmetric spread was possible, we maintained symmetric spread angles for this study. As in (19), feathers were mounted in rotational pin joints and connected to each other with tuned rubber bands (Prairie Horse Supply orthodontic elastics; one-quarter-inch medium and light force). Medium versus light force bands were tuned as needed to obtain an even distribution of feather angles as observed in pigeon tails (fig. S2). Figure S1 shows a close-up photo of the tail mechanism, showing how each DOF is transferred to the feathered planform via a universal joint.

### PigeonBot II design and fabrication

PigeonBot II combines the biohybrid morphing wing from our previous work (19) with the TailBot morphing tail. Feathers used for PigeonBot II were collected from king pigeon (*Columba livia*) cadavers purchased from Carpenter Squab Ranch in Ventura, California and Squab Producers of California from Modesto, California. The robot's feather assembly was composed of feathers from three similarly sized individuals. Secondary feathers S1 to S10 and primary feathers P1 to P7 were sourced from individual A, primary feathers P8 to P10 were from individual B, and all tail feathers were from individual C. We placed the most forward point of the tail at the wing root trailing edge to match pigeon anatomy (25). We made minor design updates to the wing from (19), which consisted of updating the wrist servomotors to slightly higher torque motors (Dymond D47), print-in-place (EOS PA 2200 Balance 1.0) wing ribs instead of balsa ribs, and symmetric motor mounts near the wing wrist joints for propulsion. We coupled the wrist and finger motion for this study as described in (19). For the wind tunnel experiments, we covered the motor mounts with 3D-printed nacelles (Ultimaker Tough PLA) for minimal aerodynamic impact on the wings. For atmospheric flights, we installed counterrotating motors and 76-mm propellers (Grem-lin 1106 4500kV and Gemfan 3035BN). The robot avionics and autopilot hardware were identical to (19) with the addition of a Teensy 4.0 Arduino as the gain scheduler and servo mixer (Fig. 1D; referred to as microcontroller). The PixRacer was updated to run ArduPilot Plane v3.9.5.

For the three-by-three wing and tail morphing postures (spread, middle, and tucked) used throughout this study, we defined the wing spread, middle, and tucked angles (biomimetic right carpometacarpus to left carpometacarpus bones) as 170°, 130°, and 90°, respectively, and the tail spread, middle, and tucked angles (outermost to outermost feathers) as 146°, 88°, and 30°, respectively (fig. S18).

We determined where to place the CG by overlaying a scaled top-down planform of PigeonBot II to fit the morphologically similar published stock dove (*Columba oenas*) outline with known CG from (43). According to the scaled outcome for PigeonBot II, we then placed the CG and rotational joint throughout this study at 24 mm behind the wing root leading edge.

### Wind tunnel (virtual flight) control loop design, testing, and tuning

We performed the wind tunnel experiments in our 1 m-by-0.82 m-by-1.73 m test section with an active turbulence grid upstream (29). We removed the top and bottom panels of the test section for mounting and access convenience. We calibrated the fan speed and active turbulence grid setpoints with a 3D ultrasonic anemometer

(Campbell CSAT3B, 100-Hz sampling). All wind tunnel results in this study were at an airspeed of 10 m/s, a value chosen to simplify this study's number of experimental variables to just one speed, within the range of gliding pigeon speeds (25), and consistent with the cruise speeds found in our previous robotic pigeon studies (3, 19). Unless otherwise indicated (such as the turbulence manipulation experiment; Fig. 4), the turbulence level was calibrated to 3% turbulence intensity. We mounted PigeonBot II in the wind tunnel via a sting extending from the top of the test section that attaches to the robot with a spherical joint (DU-BRO 2-56 threaded ball link) located at the robot CG to perform our virtual flight experiments.

We configured the control system for wind tunnel virtual flight testing as shown in fig. S6. We used the PixRacer for sensor fusion, its yaw rate controller (also known as the yaw damper), and its roll PID controller. We took the yaw and roll outputs from the PixRacer and multiplied them with mixing constants ( $K_{\text{tilt}}$ ,  $K_{\text{dev}}$ , and  $K_{\text{asym}}$ ) on the Teensy 4.0 to map to morphing servo commands.

We determined the tail elevation angles for cruise AoA settings for each three-by-three wing and tail morphing posture permutation by experimentally setting a constant tail elevation angle until the robot felt weightless in the hand in the wind tunnel and could be let go for brief moments without climbing or descending. We then recorded these cruise AoAs (table S2) and experimentally found tail elevation angles (testing different servo commands in  $\mu\text{s}$ ) that would passively enable us to achieve the three AoA setpoints: cruise, cruise +3°, and cruise -3° (fig. S9). We locked the tail elevation to its predetermined setting from this procedure during wind tunnel experiments, resulting in passive pitch stability, to eliminate confounding pitch control effects in our analysis. For the tucked wing with tucked tail case, we could not trim the AoA to a cruise angle +3° at max tail elevation, so we omitted those trials from our test schedule.

In our wind tunnel experiment, we established minimal control requirements for rudderless flight by comparing open-loop yaw and roll control, like fixed-wing RC bird models; closed-loop yaw damping ( $K_D$ ), like conventional airplanes compensating for insufficient weathercock stability; and closed-loop yaw damping ( $K_D$ ) and full roll ( $K_P$ ,  $K_I$ ,  $K_D$ ) control with our pigeon-inspired reflexive roll and yaw control loop (fig. S6). To determine the PID roll control and yaw damper gains for each wind tunnel experimental variation, we started with all gains zeroed such that all actuator movement was locked and centered. First, with no control, we tuned the yaw damper by increasing  $K_D$  until we observed oscillations, after which we halved the value to obtain the final yaw damper  $K_D$ , as recommended in (44). We then tuned the roll controller inspired by the Ziegler-Nichols method (45) for each variation by increasing  $K_P$  until we observed oscillations at the ultimate gain  $K_U$ . We then set the roll controller PID gains as follows

$$K_P = 0.6 * K_U \quad (1)$$

$$K_I = 1.2 * \frac{K_U}{T_U} * 30\% \quad (2)$$

$$K_D = 0.075 * K_U * T_U * 30\% \quad (3)$$

where we approximated  $T_U = 1$  s as the roughly observed oscillation frequency across all trials (a reasonable average estimate according to the open-loop and yaw damper + roll control residual



oscillation frequency distribution; Fig. 3B). We applied a 30% correction factor to the original Ziegler-Nichols method for  $K_I$  and  $K_D$  to get satisfactory results for our many DOFs system, likely due to nuances related to time delays and actuator dynamics. For further method details of the virtual flight tests in the wind tunnel, see Supplementary Methods.

For the turbulence experiment (Fig. 4), we induced turbulence with the active turbulence grid at progressively higher turbulence intensities (in intervals of 3% TI) for 60-s virtual flight durations. Each test started with releasing PigeonBot II at each experimental variation with the reflexive controller trying to maintain a 0° roll setpoint. This enabled determining the controllability boundary of the reflexive controller gains (with gains and mixing tuned in low turbulence; fig. S9) at which PigeonBot II's dynamics fully diverged because of turbulent perturbation. We terminated each trial when the robot went unstable, rebounding off the physical end stops of the spherical joint mount (movie S6). The controllability boundary shown in Fig. 3 is that the maximum turbulence intensity level PigeonBot II could sustain for a 30-s test duration.

### Atmospheric flight control experiments

We extended the control system that we designed, tested, and tuned in the wind tunnel (fig. S6) to make it flight ready for atmospheric flight testing. As further detailed below, in the atmospheric flight control system (Fig. 1D), the same yaw and roll control schemes from the wind tunnel were used to enable turning flight. Moreover, pitch was fully controlled (PID + feedforward) via tail elevation (Fig. 1D). To enable online calculation of appropriate gains for each teleoperated wing and tail morph combination, we implemented an adaptive gain scheduler that fits and models the gains that we tuned manually in the wind tunnel (fig. S9). The aforementioned lower-level roll, pitch, and yaw control loops ran during all flight phases, including teleoperation and autonomous navigation. Teleoperation and autonomous navigation flight modes differed only in that teleoperation allowed the teleoperator to command roll angle and either pitch angle or climb/descend rate setpoints, whereas in autonomous navigation, the navigation controller commanded these roll angle, climb/descend rate, and pitch angle setpoints. The following paragraphs detail the reflexive morphing control loop implementation, followed by the teleoperation versus autonomous navigation flight mode implementation.

When applied in the context of the autonomous circling tests (Fig. 5), we let Ardupilot's default navigation controller stream pitch and roll setpoints to our adaptive gain scheduler and mixer (Fig. 1D). Consequently, circling flight was achieved by banking the wings in roll (via wing asymmetry, tail deviation, and tail tilt), which reoriented the lift vector toward the circle center. For further details on turn coordination, pitch control, and airspeed control implementation, see Supplementary Methods.

To continuously adapt (or schedule) the roll and yaw feedback gains that modified the autopilot's output to the appropriate level according to the wing and tail morph posture and AoA, we fit two separate polynomial models of tuned wind tunnel control gains as a function of morph posture and tail elevation. Given that we already treated the combination of morph posture and tail elevation as a steady-state predictor of AoA in the wind tunnel study (table S2), these models used tail elevation angle directly (in addition to wing and tail spread) as a proxy for AoA, rather than an additional AoA estimator model. We model the scheduled roll control and yaw

damper gain using a 10-coefficient continuous function across all morph and elevation states

$$K_{\text{fit}} = C_1 \theta_{\text{tail elevation}} + C_2 \theta_{\text{wing spread}} + C_3 \theta_{\text{tail spread}} + C_4 \theta_{\text{tail elevation}}^2 + C_5 \theta_{\text{wing spread}}^2 + C_6 \theta_{\text{tail spread}}^2 + C_7 \theta_{\text{tail elevation}} * \theta_{\text{wing spread}} + C_8 \theta_{\text{tail elevation}} * \theta_{\text{tail spread}} + C_9 \theta_{\text{wing spread}} * \theta_{\text{tail spread}} + C_{10} \quad (4)$$

which resulted in a root mean square error (RMSE) of 22.9% for the roll gain and 4.8% for the yaw damper gain when evaluated at the three-by-three wing and tail spread permutations (spread, middle, and tucked) and their corresponding tail elevation angles to produce the three AoA combinations (cruise, cruise +3°, and cruise −3°). We arrived at these scheduled roll control and yaw damper gain models after fitting progressively larger linear models to our data and selecting the model that gave the lowest RMSE before visually appearing to overfit the data. We implemented these models on a Teensy 4.0 microcontroller, updating at 100 Hz. For the roll controller, we continued to run the default roll controller in Ardupilot on the PixRacer. Its roll PID output was scaled continuously on the Teensy 4.0 according to the roll gain model above throughout flight on the basis of the teleoperated wing and tail morph. Given that we ended up with the same ratios of  $K_P$ ,  $K_I$ , and  $K_D$  for roll control throughout all cases in the wind tunnel study, in Ardupilot, we simply set  $K_P = 1$  while scaling  $K_I$  and  $K_D$  appropriately as static values ( $K_I = 0.6$ ,  $K_D = 0.037$ ) to set the ratios. In contrast, we implemented the entire yaw damper controller on the Teensy 4.0, updating at 50 Hz, bypassing the Ardupilot yaw controller entirely. Combined, the PID roll and pitch control scheme fully close the loop on roll and pitch angle during atmospheric flights, whereas the yaw damping control scheme only provides damping of the yaw angle rate.

The adaptive reflexive control loop that controlled roll angle, pitch angle, and yaw angle rate ran continuously as a fly-by-wire scheme in both teleoperation and autonomous navigation flight modes. Teleoperation was flown in Ardupilot's Fly-by-Wire-A (roll and pitch angle setpoints) or Fly-by-Wire-B (roll and climb/descend rate setpoints) flight modes at the teleoperator's discretion to ensure safe flights. In the Fly-by-Wire-A mode, the teleoperator commanded the wing and tail spread angles as well as the roll and pitch angle setpoints, which fed into our adaptive reflexive morphing controller. Fly-by-Wire-B flight mode was identical to Fly-by-Wire-A mode except for the teleoperator commanding the climb/descend rate instead of the pitch angle. The climb/descend rate was then fed into the default Ardupilot total energy control system controller to be converted into a pitch angle setpoint. Because we implemented our own airspeed controller that ran the entire time, PigeonBot II ignored any throttle or airspeed control built into Ardupilot. Autonomous circular flight trajectories in Fig. 5 were performed in Ardupilot's Loiter flight mode, which replaced the teleoperator's manual roll and pitch (or climb/descend rate) setpoints with Ardupilot's default navigation controller—which outputs pitch and roll angle setpoints to the same adaptive reflexive morphing controller as in every other flight mode.

### Statistical analysis

We calculated the  $RMS_{\text{roll-yaw}}$  in Fig. 2D by taking the RMS of the resultant roll and yaw angle vectors from each wind-tunnel trial

$$RMS_{\text{roll-yaw}} = RMS\left(\sqrt{\theta_{\text{roll}}^2 + \theta_{\text{yaw}}^2}\right) \quad (5)$$



Further details on the lengths of these wind tunnel trials are in Supplementary Methods.

For the roll, pitch, and yaw SD results shown in Fig. 4A, we took the SD of the recorded roll, pitch, and yaw angles for 30 s. We only plotted traces up to where PigeonBot II could remain stable for the entire 30-s trial duration.

In atmospheric flight experiments, we assessed the circular flight performance by calculating the mean radius and SD by first fitting the loiter data to a circle to find the circle center (46) and then calculating the 2D projected lateral distance to the fitted circle center throughout the trial. We trimmed the circle flight trials in Fig. 5 (B and C) to 30 s, unless the flown trials were already shorter than 30 s, to more equally weight and compare the radii flown (Fig. 5C). Flight durations are shown in Fig. 5B.

The turbulence intensities reported for atmospheric flights (figs. S13 to S15) were calculated from onboard Pitot tube airspeed data, sampled at 25 Hz. We calculated the turbulence intensity by taking a moving SD of the airspeed and dividing by a moving average of the airspeed. The moving average window was 2 s.

## Supplementary Materials

The PDF file includes:

Methods  
Figs. S1 to S18  
Tables S1 and S2  
References (48–73)

Other Supplementary Material for this manuscript includes the following:

Movies S1 to S7

## REFERENCES AND NOTES

- C. J. Pennycuik, *Modelling the Flying Bird* (Elsevier Science, 2008).
- D. D. Chin, L. Y. Matloff, A. K. Stowers, E. R. Tucci, D. Lentink, Inspiration for wing design: How forelimb specialization enables active flight in modern vertebrates. *J. R. Soc. Interface* **14**, 20170240 (2017).
- L. Y. Matloff, E. Chang, T. J. Feo, L. Jeffries, A. K. Stowers, C. Thomson, D. Lentink, How flight feathers stick together to form a continuous morphing wing. *Science* **367**, 293–297 (2020).
- S. Watanabe, S. Sunada, K. Yamaguchi, Optimization of high-crosswind-tolerant airplane based on double-hinged-wing and no-vertical-tail configuration. *Trans. Jpn. Soc. Aeronaut. Space Sci.* **66**, 70–82 (2023).
- R. C. Nelson, *Flight Stability and Automatic Control* (WCB/McGraw Hill, 1998), vol. 2.
- J. D. Anderson, *A History of Aerodynamics: And Its Impact on Flying Machines* (Cambridge Univ. Press, 1998), vol. 8.
- K. Nickell, M. Wohlfahrt, E. Brown, *Tailless Aircraft in Theory and Practice* (Edward Arnold, 1994).
- W. F. Phillips, *Mechanics of Flight* (John Wiley & Sons, 2004).
- R. Horten, P. F. Selinger, *Nurflügel: Die Geschichte Der Horten-Flugzeuge 1933–1960* (Weishaupt, 1987).
- A. H. Bowers, O. J. Murillo, R. Jensen, B. Eslinger, C. Gelzer, “On wings of the minimum induced drag: Spanload implications for aircraft and birds” (NASA, 2016).
- D. Bilo, “Course control during flight” in *Perception and Motor Control in Birds* (Springer, 1994), pp. 227–247.
- J. H. Storer, Flight of birds analyzed through slow-motion photography. *Condor* **51**, 276–277 (1949).
- A. Jack, *Feathered Wings: A Study of the Flight of Birds* (Methuen & Co., 1953).
- R. H. J. Brown, The flight of birds. *Biol. Rev.* **38**, 460–489 (1963).
- H. Oehme, Die flugsteuerung des vogels. I. Ueber flugmechanische grundlagen. *Beitr Vogelkd.* **22**, 58–66 (1976).
- J. J. Baume, *Functional Morphology of the Tail Apparatus of the Pigeon (Columba livia)* (Springer, 1988).
- K. L. McArthur, J. D. Dickman, State-dependent sensorimotor processing: Gaze and posture stability during simulated flight in birds. *J. Neurophysiol.* **105**, 1689–1700 (2011).
- F. Groebbels, Der Vogel als automatisch sich steuerndes Flugzeug. *Naturwissenschaften* **17**, 890–893 (1929).
- E. Chang, L. Y. Matloff, A. K. Stowers, D. Lentink, Soft biohybrid morphing wings with feathers underactuated by wrist and finger motion. *Sci. Robot.* **5**, eaay1246 (2020).
- M. Bras, J. Vale, F. Lau, A. Suleman, Flight dynamics and control of a vertical tailless aircraft. *J. Aeronaut. Astronaut. Eng.* **2**, 1–10 (2013).
- Y. Murayama, T. Nakata, H. Liu, Aerodynamic performance of a bird-inspired morphing tail. *J. Biomech. Sci. Eng.* **18**, 22-00340 (2023).
- R. G. Hoey, Exploring bird aerodynamics using radio-controlled models. *Bioinspiration Biomim.* **5**, 045008 (2010).
- G. Sachs, Why birds and miniscale airplanes need no vertical tail. *J. Aircr.* **44**, 1159–1167 (2007).
- J. A. Gillies, A. L. Thomas, G. K. Taylor, Soaring and manoeuvring flight of a steppe eagle *Aquila nipalensis*. *J. Avian Biol.* **42**, 377–386 (2011).
- C. J. Pennycuik, A wind-tunnel study of gliding flight in the pigeon *Columba livia*. *J. Exp. Biol.* **49**, 509–526 (1968).
- D. Lentink, “Exploring the biofluidynamics of swimming and flight,” thesis, Wageningen University, 2008.
- E. Ajanić, M. Feroskhan, S. Mintchev, F. Noca, D. Floreano, Bioinspired wing and tail morphing extends drone flight capabilities. *Sci. Robot.* **5**, eabc2897 (2020).
- L. Jeffries, D. Lentink, Design principles and function of mechanical fasteners in nature and technology. *Appl. Mech. Rev.* **72**, 050802 (2020).
- D. B. Quinn, A. Watts, T. Nagle, D. Lentink, A new low-turbulence wind tunnel for animal and small vehicle flight experiments. *R. Soc. Open Sci.* **4**, 160960 (2017).
- D. Lentink, U. K. Muller, E. J. Stamhuis, R. de Kat, W. van Gestel, L. L. Veldhuis, P. Henningson, A. Hedenstrom, J. J. Videler, J. L. van Leeuwen, How swifts control their glide performance with morphing wings. *Nature* **446**, 1082–1085 (2007).
- J. H. Storer, “The flight of birds analyzed through slow-motion photography” (Cranbrook Institute of Science, 1948).
- C. Harvey, V. B. Baliga, J. C. M. Wong, D. L. Altshuler, D. J. Inman, Birds can transition between stable and unstable states via wing morphing. *Nature* **603**, 648–653 (2022).
- A. Schmidt, B. Feldotto, T. Gumpert, D. Seidel, A. Albu-Schäffer, P. Stratmann, Adapting highly-dynamic compliant movements to changing environments: A benchmark comparison of reflex- vs. CPG-based control strategies. *Front. Neurobot.* **15**, 762431 (2021).
- D. H. Myszk, J. J. Joo, A. P. Murray, A multi-objective mechanism optimization for controlling an aircraft using a bio-inspired rotating empennage. *J. Mech. Robot.* **14**, 045003 (2022).
- L. Begin, “The Northrop Flying Wing prototypes” in *Aircraft Prototype and Technology Demonstrator Symposium* (American Institute of Aeronautics and Astronautics, 1983).
- W. Sears, “Flying-wing airplanes - The XB-35/YB-49 program” in *The Evolution of Aircraft Wing Design: Proceedings of the Symposium* (American Institute of Aeronautics and Astronautics, 1980).
- D. Quinn, D. Kress, E. Chang, A. Stein, M. Wegrzynski, D. Lentink, How lovebirds maneuver through lateral gusts with minimal visual information. *Proc. Natl. Acad. Sci. U.S.A.* **116**, 15033–15041 (2019).
- A. A. Paranjape, S.-J. Chung, M. S. Selig, Flight mechanics of a tailless articulated wing aircraft. *Bioinspiration Biomim.* **6**, 026005 (2011).
- A. E. Bryson, *Applied Optimal Control: Optimization, Estimation and Control* (Routledge, 2017).
- C. Harvey, G. de Croon, G. K. Taylor, R. J. Bomphrey, Lessons from natural flight for aviation: then, now and tomorrow. *J. Exp. Biol.* **226**, jeb245409 (2023).
- S. M. Gatesy, K. P. Dial, Tail muscle activity patterns in walking and flying pigeons (*Columba livia*). *J. Exp. Biol.* **176**, 55–76 (1993).
- A. A. Biewener, Muscle function in avian flight: Achieving power and control. *Philos. Trans. R. Soc. B: Biol. Sci.* **366**, 1496–1506 (2011).
- A. L. R. Thomas, G. K. Taylor, Animal flight dynamics I. Stability in gliding flight. *J. Theor. Biol.* **212**, 399–424 (2001).
- ArduPilot Dev Team, Roll, pitch and yaw controller tuning; <https://ardupilot.org/plane/docs/roll-pitch-controller-tuning.html>.
- J. G. Ziegler, N. B. Nichols, Optimum settings for automatic controllers. *Trans. Am. Soc. Mech. Eng.* **64**, 759–765 (1942).
- I. Bucher, Circle fit (1981); [www.mathworks.com/matlabcentral/fileexchange/5557-circle-fit](http://www.mathworks.com/matlabcentral/fileexchange/5557-circle-fit).
- D. B. Quinn, Y. van Halder, D. Lentink, Adaptive control of turbulence intensity is accelerated by frugal flow sampling. *J. R. Soc. Interface* **14**, 20170621 (2017).
- M. Dreila, H. Youngren, AVL (Athena Vortex Lattice) (2007); <https://web.mit.edu/dreila/Public/web/avl/>.
- M. Dreila, H. Youngren, M. Scherrer, A. Depierreux, XFLR5 v6.61 (2023); <http://www.xflr5.tech>.
- M. Dreila, “XFoil: An analysis and design system for low Reynolds number airfoils” in *Low Reynolds Number Aerodynamics*, T. J. Mueller, Ed. (Springer, 1989), pp. 1–12.

51. B. Etkin, T. Teichmann, Dynamics of flight: Stability and control. *Phys. Today* **12**, 54–56 (1959).
52. H.-V. Phan, D. Floreano, Raptor-informed feathered drone reveals tail-twist functions in avian turning manoeuvres. *bioRxiv* 573672 [Preprint]. 30 December 2023. <https://doi.org/10.1101/2023.12.29.573672>.
53. H. Garcia, M. Abdulrahim, R. Lind, "Roll control for a micro air vehicle using active wing morphing" in *AIAA Guidance, Navigation, and Control Conference and Exhibit* (American Institute of Aeronautics and Astronautics, 2003).
54. M. Abdulrahim, H. Garcia, G. Ivey, R. Lind, "Flight testing a micro air vehicle using morphing for aeroservoelastic control" in *45th AIAA/ASME/ASCE/AHS/ASC Structures, Structural Dynamics, and Materials Conference* (American Institute of Aeronautics and Astronautics, 2004).
55. M. Abdulrahim, R. Lind, "Flight testing and response characteristics of a variable gull-wing morphing aircraft" in *AIAA Guidance, Navigation, and Control Conference and Exhibit* (American Institute of Aeronautics and Astronautics, 2010).
56. R. Guiler, W. Huebsch, "Wind tunnel analysis of a morphing swept wing tailless aircraft" in *23rd AIAA Applied Aerodynamics Conference* (American Institute of Aeronautics and Astronautics, 2005).
57. D. T. Grant, M. Abdulrahim, R. Lind, Flight dynamics of a morphing aircraft utilizing independent multiple-joint wing sweep. *Int. J. Micro Air Veh.* **2**, 91–106 (2010).
58. D. Tran, R. Lind, "Parameterizing stability derivatives and flight dynamics with wing deformation" in *AIAA Atmospheric Flight Mechanics Conference* (American Institute of Aeronautics and Astronautics, 2010).
59. G. Molinari, A. F. Arrieta, M. Guillaume, P. Ermanni, Aerostructural performance of distributed compliance morphing wings: Wind tunnel and flight testing. *AIAA J.* **54**, 3859–3871 (2016).
60. R. Siddall, M. Kovac, Fast aquatic escape with a jet thruster. *IEEE/ASME Trans. Mechatron.* **22**, 217–226 (2017).
61. M. Di Luca, S. Mintchev, G. Heitz, F. Noca, D. Floreano, Bioinspired morphing wings for extended flight envelope and roll control of small drones. *Interface Focus* **7**, 20160092 (2017).
62. Z. Hui, Y. Zhang, G. Chen, Aerodynamic performance investigation on a morphing unmanned aerial vehicle with bio-inspired discrete wing structures. *Aerosp. Sci. Technol.* **95**, 105419 (2019).
63. A. Zhao, H. Zou, H. Jin, D. Wen, Structural design and verification of an innovative whole adaptive variable camber wing. *Aerosp. Sci. Technol.* **89**, 11–18 (2019).
64. K. Wright, "Investigating the use of wing sweep for pitch control of a small unmanned air vehicle," thesis, University of California, San Diego, CA (2011).
65. A. A. Paranjape, S.-J. Chung, J. Kim, Novel dihedral-based control of flapping-wing aircraft with application to perching. *IEEE Trans. Robot.* **29**, 1071–1084 (2013).
66. Z. R. Manchester, J. I. Lipton, R. J. Wood, S. Kuindersma, "A variable forward-sweep wing design for enhanced perching in micro aerial vehicles" in *55th AIAA Aerospace Sciences Meeting* (American Institute of Aeronautics and Astronautics, 2017).
67. R. Siddall, A. Ortega Ancel, M. Kovac, Wind and water tunnel testing of a morphing aquatic micro air vehicle. *Interface Focus* **7**, 20160085 (2017).
68. C. Greatwood, A. Wallock, T. Richardson, Perched landing manoeuvres with a variable sweep wing UAV. *Aerosp. Sci. Technol.* **71**, 510–520 (2017).
69. P. Ortiz, N. Alley, "Spanwise adaptive wing-PTERA flight test" in *AIAA Aviation Forum* (American Institute of Aeronautics and Astronautics, 2018).
70. J. R. Parga, M. F. Reeder, T. Leveron, K. Blackburn, Experimental study of a micro air vehicle with a rotatable tail. *J. Aircr.* **44**, 1761–1768 (2007).
71. F. Nickols, Y. J. Lin, "Feathered tail and pygostyle for the flying control of a bio-mimicking eagle bird robot" in *2017 IEEE International Conference on Cybernetics and Intelligent Systems (CIS) and IEEE Conference on Robotics, Automation and Mechatronics (RAM)* (IEEE, 2017), pp. 556–561.
72. L. Zheng, Z. Zhou, P. Sun, Z. Zhang, R. Wang, A novel control mode of bionic morphing tail based on deep reinforcement learning. *arXiv:2010.03814 [physics.flu-dyn]* (8 October 2020).
73. E. Ajanic, M. Feroskhan, V. Wüest, D. Floreano, Sharp turning maneuvers with avian-inspired wing and tail morphing. *Commun. Eng.* **1**, 34 (2022).

**Acknowledgments:** We thank W. Roderick for fruitful discussions during this research and for reviewing this manuscript, K. Hoffmann for assistance with atmospheric flights, and E. Barber for initial work on aerodynamic simulations. **Funding:** This work was supported by the EOARD/AFOSR award numbers FA8655-22-1-7053 and FA9550-18-1-0525 with special thanks to D. D. Swanson and B. L. Lee for monitoring the program (to D.L.) and NSF GRFP Fellowship (to E.C.). **Author contributions:** Conceptualization: D.L. and E.C. Methodology: E.C. and D.L. Investigation: E.C. and D.L. Visualization: E.C. and D.L. Funding acquisition: D.L. Supervision: D.L. Writing—original draft: D.L. Writing—review and editing: E.C., D.L., and D.D.C. **Competing interests:** The authors declare that they have no competing interests. **Data and materials availability:** Wind tunnel data, dynamic simulation data, and a computer-aided design (CAD) model of PigeonBot II have been deposited on Dryad at <https://doi.org/10.5061/dryad.zkh1893h5>. All remaining data are available in the paper or the Supplementary Materials.

Submitted 2 February 2024  
 Accepted 21 October 2024  
 Published 20 November 2024  
 10.1126/scirobotics.ado4535